Barium-Based Manganites $Ln_{1-x}Ba_xMnO_3$ with Ln = {Pr, La}: Phase Transitions and Magnetoresistance Properties

A. Barnabé, F. Millange, A. Maignan, M. Hervieu,* and B. Raveau

Laboratoire CRISMAT, ISMRA Université de Caen, 6 Boulevard du Maréchal Juin, 14050 Caen Cedex, France

G. Van Tendeloo and P. Laffez

RUCA, EMAT, groenenborgerlaan, University of Antwerpen, Antwerpen, Belgium

Received June 4, 1997. Revised Manuscript Received September 10, 1997[⊗]

Using a "two-steps" synthesis mode, the homogeneity ranges of the perovskites $Ln_{1-x}Ba_xMnO_3$ were extended up to $x = 0.60$ for the Pr-based samples and $x = 0.50$ for the La ones. Two new perovskites, a cubic form and a P-type tetragonal phase (with $a_C \times a_C \times 2a_C$ parameters) have been isolated. The HREM study shows a nanostructural behavior of the new tetragonal form, only stabilized in small domains. These compounds exhibit a ferromagnetic metallic to paramagnetic insulating transition at increasing temperature, over a large homogeneity range, independent of the nature of the perovskite structure. Consequently, magnetoresistance effects are observed. The Curie temperature reaches values as high as 362 K and goes though a maximum. These properties are discussed considering three factors—size, valence, and mismatch effects—which are known to govern the CMR properties of the manganites.

Introduction

Since the discovery by Kusters et al.[1] of magnetoresistance properties in $Ln_{1-x}A_xMnO_3$, manganites exhibiting the perovskite structure have been extensively studied for A = Ca, Sr. The $Ln_{1-x}Ba_xMnO_3$ systems however have received much less attention, although thin films of the phase $La_{0.66}Ba_{0.33}MnO_3$ exhibit a large magnetoresistance effect, typically a resistance ratio R_0/R_H of 50% at 290 K in a magnetic field of 5 T.[2,3] Actually, only lanthanide rich phases ($x < 0.4$) have been studied up to now, as shown for Ln = Pr, La.[4−6] This can be obviously related to the difficulty to isolate single-phase materials in the barium-rich region, due to the easy formation of $BaMnO_3$ in air.

In the present study the Pr and La barium manganites are revisited using a different synthetic method in order to extend their homogeneity range. A detailed high electron microscopy investigation is performed in order to understand the complex phase transitions that appear as a function of composition for these compounds. The magnetotransport properties of these compounds, which exhibit to date the highest T_C, up to 362 K, are studied and discussed in the light of their crystal chemistry.

Experimental Section

The manganese perovskites were prepared by mixing the oxides La_2O_3 or Pr_6O_{11}, MnO_2, and the carbonate $BaCO_3$ in stoichiometric proportions. The mixtures were first heated to achieve decarbonation. The resulting powders were pressed into the form of pellets under 1 ton cm^{-2} pressure and sintered at $T = 1500$ °C for 12 h in an argon flux in order to avoid the complete oxidization of Mn(III) into Mn(IV), which would favor the formation of $BaMnO_3$. The products are then slowly cooled to room temperature in the same atmosphere. Finally, the pellets were annealed at $T \approx 600$ °C in oxidizing atmosphere (air or O_2 flux) in order to optimize the oxygen content of the samples. Iodometric titration indicates that the oxygen stoichiometry of the samples is close to 3.00 with an accuracy of ±0.02. The analysis of the phase and determination of the lattice parameters were carried out from diffraction data registered with a Philips diffractometer using Cu Kα radiation.

The electron diffraction study was performed with a JEOL 200CX and a Philips CM20 electron microscope equipped with a side entry goniometer (±60°). The high-resolution microscopy study was carried out with a TOPCON 002B microscope and a JEOL 4000EX microscope. Image calculations have been carried out with the Mac Tempas program. EDS analyses were systematically performed on numerous grains. They confirmed the homogeneity of the cation distribution within the crystals, corresponding to the nominal composition of the samples.

Powder neutron diffraction data were collected on the high-resolution diffractometer D2B (ILL, Grenoble) at room temperature with a wavelength of $\lambda = 1.5938$ Å. Data in the range

[⊗] Abstract published in *Advance ACS Abstracts,* November 15, 1997.

(1) Kusters, R. M.; Singleton, J.; Keen, D. A.; Greevy, R. M.; Hayes, W. *Physica B* **1989**, *155*, 362.
(2) Von Helmolt, R.; Wecker, J.; Holzapfel, B.; Schultz, L.; Samwer, K. *Phys. Rev. Lett.* **1993**, *71*, 2331.
(3) Xiong, G. C.; Li, Q.; Ju, H. L.; Greene, R. L.; Venkatesan, T. *Appl. Phys. Lett.* **1995**, *66*, 13.
(4) Jirak, Z.; Pollert, E.; Andersen, A. F.; Grenier, J. C.; Hagenmuller, P. *Eur. J. Solid. State Inorg. Chem.* **1990**, *27*, 421−433.
(5) Radaelli, P. G.; Marezio, M.; Hwang, H. Y.; Cheong, S. W. *J. Solid State Chem.* **1996**, *122*, 444−447.
(6) Ju, H. L.; Gopalakrishnan, J.; Peng, J. L.; Xiong, G. C.; Venkatesan, T.; Greene, R. L. *Phys. Rev. B* **1994**, *51*, 6143.

S0897-4756(97)00408-0 CCC: $15.00
Published on Web 01/19/1998

Table 1. Atomic Positions and Cell Parameters

(a) $Pr_{1-x}Ba_xMnO_3$

$Pr_{1-x}Ba_xMnO_3$	$x = 0.50$	$x = 0.60$
space group	$Pm3m$	$Pm3m$
parameters	3.8949(3)	3.897(4)
R_I factor	3%[a]	10%
Mn	$^1/_2$ $^1/_2$ $^1/_2$	$^1/_2$ $^1/_2$ $^1/_2$
Pr/Ba	0 0 0	0 0 0
O	0 $^1/_2$ $^1/_2$	0 $^1/_2$ $^1/_2$

(b) $La_{1-x}Ba_xMnO_3$

$La_{1-x}Ba_xMnO_3$	$x = 0.20$	$x = 0.30$	$x = 0.50$
space group	$R\bar{3}c$	$R\bar{3}c$	$Pm3m$
parameters	5.556(2)	5.539(3)	3.908(1)
	13.470(8)	13.504(6)	
R_I factor	5.9%	4.8%	2.1%
Mn	0 0 0	0 0 0	$^1/_2$ $^1/_2$ $^1/_2$
La/Ba	0 0 $^1/_4$	0 0 $^1/_4$	0 0 0
O	0.454(3) 0 $^1/_4$	0.468(1) 0 $^1/_4$	$^1/_2$ $^1/_2$ 0

(c) Phases Diagrams of $La_{1-x}Ba_xMnO_3$ and $Pr_{1-x}Ba_xMnO_3$

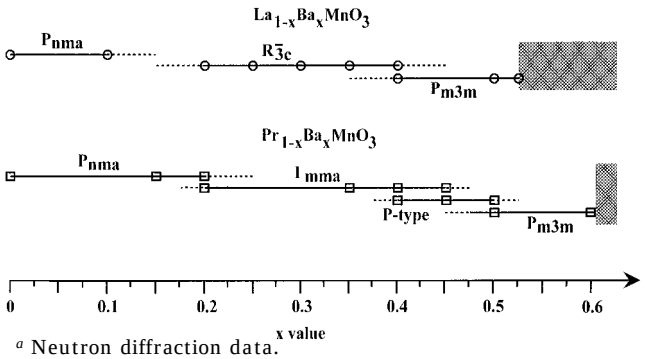

[a] Neutron diffraction data.

$15° \leq 2\theta \leq 160°$ were refined by the Rietveld method using the program Fullprof.

Magnetization measurements were performed after zero field cooling from 5 to 400 K using a SQUID magnetometer and a vibrating sample magnetometer.

Resistivity was measured between 5 and 400 K, on bars with dimensions $0.2 \times 0.2 \times 1$ cm^3, using a standard four-point method. Magnetoresistance measurements were performed in a magnetic field up to 7 T with temperatures ranging from 5 to 300 K.

Structural Transitions

Following the above experimental procedure, i.e., using Ar in the first step and reoxidizing the samples in a second step, the homogeneity ranges of the perovskites $Ln_{1-x}Ba_xMnO_3$ were extended up to $x = 0.60$ for the Pr-based samples and $x = 0.50$ for the La ones. The composition and structure of the Ba content samples were determined in order to confirm the reliability of the synthesis method. They were similar to samples previously synthesized directly in air. In the case of lanthanum, the $R\bar{3}c$ structure previously obtained by Radaelli et al.[5] is observed for $0.20 \leq x \leq 0.40$. In the case of praseodymium, one obtains for $0 \leq x \leq 0.35$, two phases with the space groups $Pnma$ (for $0 \leq x \leq 0.20$) and $Imma$ (for $0.20 \leq x \leq 0.35$) in agreement with Jirak et al.[4] For $0.40 \leq x \leq 0.50$ and for $0.40 \leq x \leq 0.60$, respectively, two new perovskites are obtained as well for La as for Pr, whereas for $x > 0.60$, one observes the formation of the 6L $BaMnO_3$ structure.[7]

(7) Negas, T.; Roth, R. S. *J. Solid State Chem.* **1971**, *3*, 323−339.

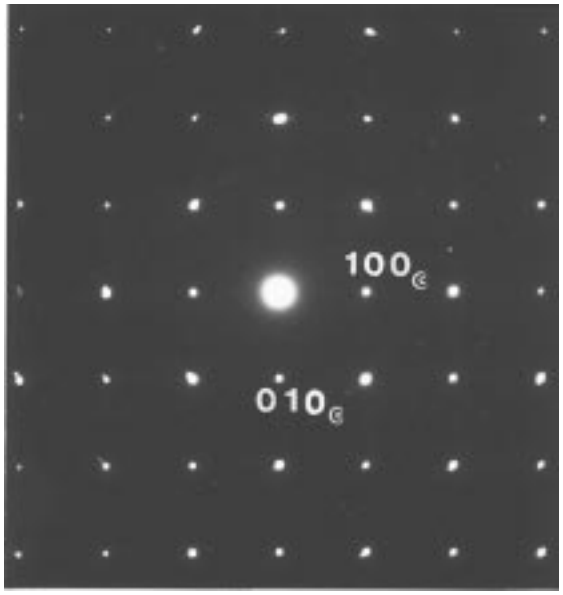

Figure 1. [001] ED pattern of the cubic perovskite $Pr_{0.40}Ba_{0.60}MnO_3$.

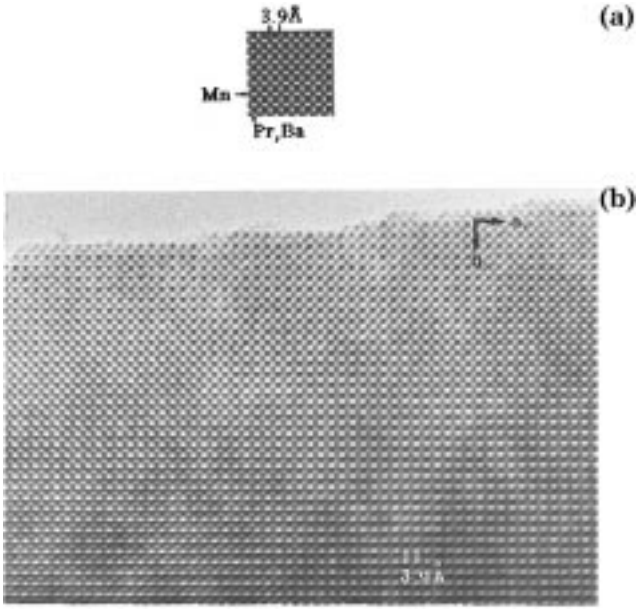

Figure 2. (a) Simulated and (b) HREM images of the cubic perovskite $Pr_{0.40}Ba_{0.60}MnO_3$.

Cubic Perovskite $Ln_{1-x}Ba_xMnO_3$. The XRD patterns of the phases $Pr_{1-x}Ba_xMnO_3$ for $0.55 \leq x \leq 0.60$ and $La_{1-x}Ba_xMnO_3$ for $0.45 \leq x \leq 0.50$ can be indexed as cubic, all with the following parameters (Table 1): $a_c = 3.8950(1)$ Å for $Pr_{0.45}Ba_{0.55}MnO_3$, $a_c = 3.8974(1)$ Å for $Pr_{0.40}Ba_{0.60}MnO_3$, $a_c = 3.9065(1)$ Å for $La_{0.55}Ba_{0.45}MnO_3$, and $a_c = 3.9081(1)$ Å for $La_{0.50}Ba_{0.50}MnO_3$. The reconstruction of the reciprocal space from the ED patterns of these oxides tilting around the $[001]_c^*$ (Figure 1) and $[110]_c^*$ directions confirms the cubic structure. The comparison of the experimental and calculated HREM images (Figure 2a,b, for a focus value close to −900 Å so that the cation positions are imaged as dark spots) confirm that the microcrystals exhibit a perfect perovskite structure.

The iodometric titration shows the O_3 stoichiometry for all these compositions.

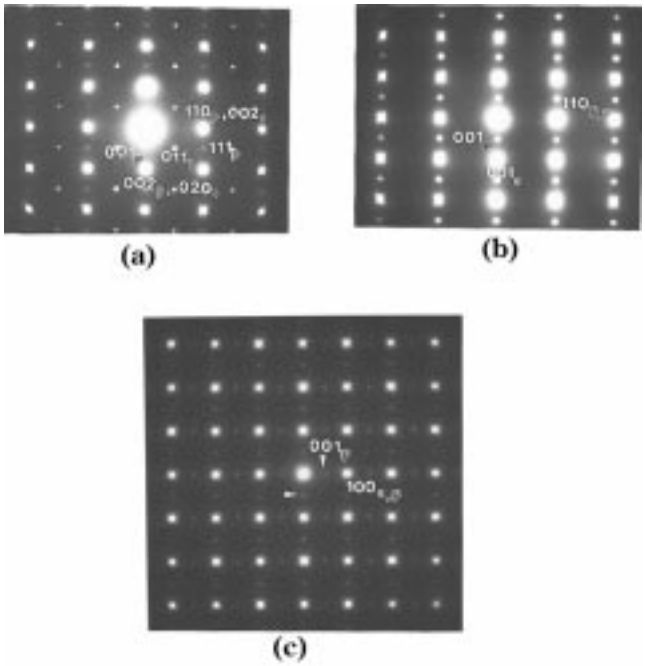

Figure 3. ED patterns of the perovskite $Pr_{1-x}Ba_xMnO_3$. **3a**: Coexistence of the P-type double perovskite and *Imma* one for the chemical composition close to $x = 0.40$. **3b**: Typical $[1\bar{1}0]_P$ ED pattern of $Pr_{0.50}Ba_{0.50}MnO_3$. **3c**: $[010]_I$ zone of the *Imma* structure or $[100]_C$ zone of the P-type double-perovskite phase.

Intermediate Phase $Pr_{1-x}Ba_xMnO_3$: $0.40 < x < 0.55$. The XRD patterns of $Pr_{1-x}Ba_xMnO_3$ ($0.40 < x < 0.55$) indicate that the materials are single phased. However, the electron diffraction study shows the coexistence of two perovskite phases. Over the whole composition range $0.40 < x < 0.55$, and within every grain, a new perovskite coexists either with the *Imma* structure ($x \approx 0.40$) or with the cubic perovskite ($x > 0.45$). This new phase exhibits a double perovskite cell with $a_P \approx b_P \approx a_c$ and $c_P \approx 2a_c$ and with a P-type lattice. The index **P** is used to describe this tetragonal double perovskite cell; the suffix **I** indicates the *Imma* structure.

For x values close to 0.40, the double perovskite coexists with the *Imma* structure. This is illustrated in the ED pattern of Figure 3a, where the intense reflections are those of the *Imma* phase. In this $[100]_I$ pattern, weak and diffuse reflections appears along b_I^*, for $k = 2n + 1$, which are not compatible with the I-type lattice.

For x values ranging between 0.45 and 0.55, the I-type lattice reflections are no longer observed. The intense reflections are those of the cubic perovskite and the additional spots are characteristic of the doubling of the c_c axis. A typical selected area (SAED) pattern of the $[1\bar{1}0]_P$ zone from the $Pr_{0.50}Ba_{0.50}MnO_3$ sample is shown in Figure 3b.

Figure 3c is a common pattern observed over the whole $0.40 < x < 0.55$ domain. It can be indexed as the $[010]_I$ zone of the *Imma* structure ($x \approx 0.40$) or to the $[010]_c$ zone of the cubic structure. The additional weak spots (indicated by a small white arrow) are the signature of the P-type double-perovskite phase. They are observed along $[101]_I^*$ and $[\bar{1}01]_I^*$ in the $x \approx 0.4$ sample or along the equivalent $[100]_c^*$ for $x \approx 0.50$. These observations confirm the presence of three different orientation variants, with the tetragonal $2a_c$ superstructure formed along every equivalent $[100]_c$ directions of the cubic perovskite subcell.

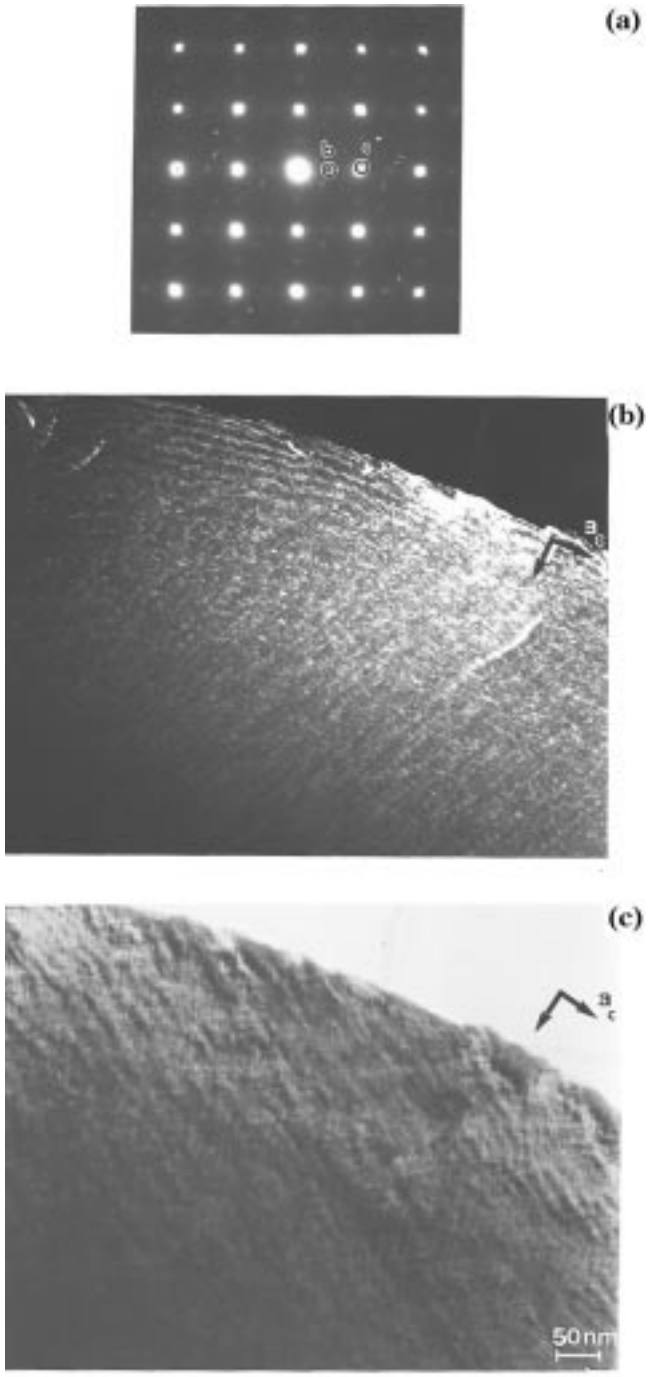

Figure 4. ED patterns and EM images of the perovskite $Pr_{1-x}Ba_xMnO_3$. **4a**: ED pattern with the selected $(100)_P$ and $(001)_P$ reflections (circled and labeled *c* and *b*). **4b**: Dark-field image selecting $(100)_P$ reflection (circle labeled *c* in Figure 4a) **4c**: Bright-field image selecting $(001)_P$ reflection (circle labeled *b* in Figure 4a).

The overall symmetry of all $[100]_c$ patterns with the double perovskite present is 4-fold; all Bragg reflections of the perovskite subcell exhibit diffuse streaks extending along the $[110]_P^*$ and $[1\bar{1}0]_P^*$ directions. This suggests the existence of ill-defined planar defects or of a tetragonal (or orthorhombic) distortion of the perovskite subcell. In contrast, the additional reflections $(0kl)_P$ resulting from the doubling of the c_c param-

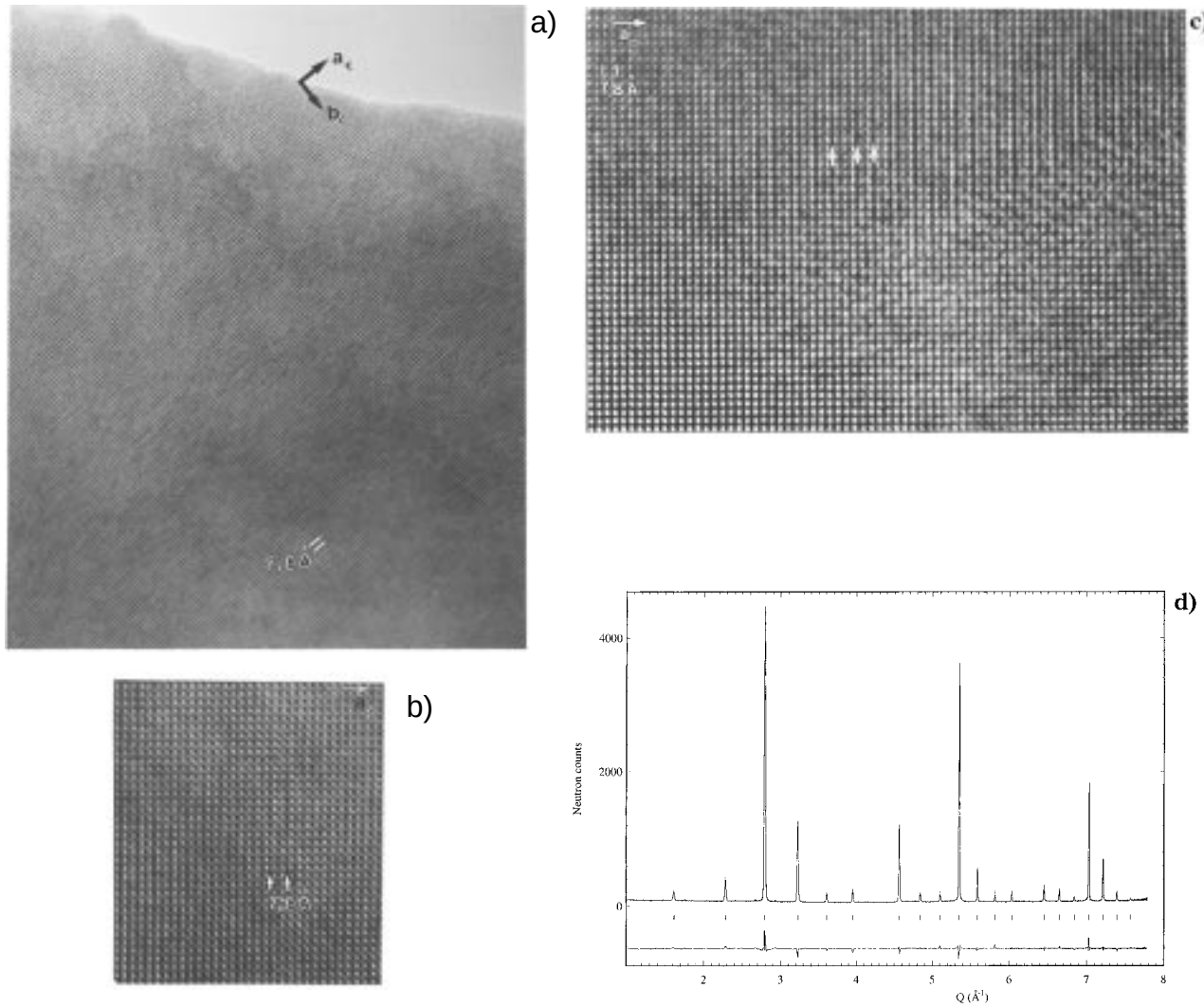

Figure 5. HREM images of $Pr_{0.50}Ba_{0.50}MnO_3$. **5a**: [001] HREM image. **5b**: Enlargement image of 5a. **5c**: HREM image of large P-type structure domain. **5d:** Rietveld refinement plot of the neutron diffraction data. Observed, calculated, and difference profiles are plotted on the same scale. The Bragg peaks are indicated by tick marks.

eter are relatively isotropic and spherical. The streaking remains by tilting around the $[100]_P$* direction, however, due to the systematic superposition of the double perovskite with *Imma* or cubic structures and due to the presence of the oriented variants, it appears to be very complex to determine the exact shape of the diffuse intensity for a single variant from diffraction evidence only. Direct imaging will help to overcome this problem.

To determine the way the distribution of the different variants within the grains and to understand the origin of the streaking, dark-field images are recorded, selecting one $(100)_P$ reflection (noted c in pattern of Figure 4a) and one $(001)_P$ reflection (noted b in pattern of Figure 4a). In the first case (Figure 4b), one observes a tweedlike contrast, with striations along $[110]_P$ and $[1\bar{1}0]_P$, the average tweed spacing being about 20 nm. In the second case (Figure 4c), one observes very small bright zones, a few nanometers large, regularly distributed throughout the crystal.

These results suggest that the double perovskite P-type structure creates a strain field within the basic perovskite structure. The tweed structure in real space is clearly related to the presence of small ordered domains (with $a = b = 3.9$ Å close but a slightly different $c/2$).

Considering the cationic composition of the sample, close to $Pr_{0.50}Ba_{0.50}Mn$, the origin of the superstructure could be correlated either to cation orderings (Pr and Ba or Mn^{3+} and Mn^{4+}) and/or to oxygen vacancies as in the so-called "112" $YBaFeCuO_5$ structure.[8] Neutron diffraction data indicate that the oxygen stoichiometry of the Ba-rich phases remains close to O_3 so that the oxygen deficiency, if any, should be very low. Various annealings were carried out on the $Pr_{0.50}Ba_{0.50}MnO_3$ sample, varying the atmosphere (Ar, air, and O_2), the temperature (between 400 and 900 °C), the annealing time (from 2 h to 15 days), and the way temperature is decreased (from quenching to a slow decrease). All of these samples were investigated by ED. The intensity of the double-perovskite reflections varies, but it remains present in all samples. None of these different thermal treatments resulted in the formation of large domains of the double-perovskite phase, which would allow an accurate structure refinement from XRD or

(8) Er Rakho, L.; Michel, C.; Lacorre, P.; Raveau, B. *J. Solid State Chem.* **1988**, *73*, 531−535.

neutron data. These experiments make it very improbable that the superstructure would be due to the formation of an $A_2Mn_2O_5$ oxygen-deficient phase.[9]

The [100] HREM images, recorded for the composition $x = 0.50$, confirm that the superstructure is formed in small domains, a few nanometers wide, with three mutually perpendicular variants and randomly distributed throughout the grains. This is illustrated in the low-magnification image of Figure 5a, where the positions of the cations are imaged as bright spots. The contrast variations introduced by the superstructure consist in the appearance of a double period, characterized by short brighter and darker segments, spaced by 7.8 Å. In the enlarged image (Figure 5b) recorded for a focus value where the Ba and Pr positions are imaged as dark spots and the manganese positions as gray spots, tiny variations of the rows spacing at the level of the [MnO_2] layers; this clearly appears by viewing at grazing incidence. These images seem to indicate that the superstructure is related to small atomic displacements along one of the cubic axes of the perovskite structure, rather than to an ordering of one of the cations.

Depending on the thermal treatment, the superstructure reflections are not always perfectly sharp; often they are streaked or have secondary maxima at incommensurate positions. In real space this means that the superstructure does not strictly correspond to a doubling of the basic unit cell. The HREM image of Figure 5c shows a large domain of about 20 nm. The contrast is similar to that detailed in Figure 5b but locally one observes a sequence with a triple period rather than the expected double period (indicated by white arrows in Figure 5c). Such translation defects or stacking disorder is responsible for the streaking of the superstructure reflections or the maxima at incommensurate positions.

The structural study was attempted from neutron diffraction data, for an $x = 0.50$ sample (Figure 5d). Though the ED characterization confirmed the coexistence of the tetragonal and cubic phases, the ratio $2a/c$ of the tetragonal phase is too close to 1 so that the refinements can only be carried out for a cubic cell with $a = 3.8949(3)$ Å. However, it confirms the oxygen content close to 3.00/perovskite cell.

The cell parameters only slightly alter over the existence domain of the double-perovskite structure, up to $x = 0.60$ where the "perfect cubic structure" is reached. This means that the difference between the Ba and Pr radii is almost perfectly compensated by that between the Mn^{3+} and Mn^{4+} for a constant oxygen content of O_3.

Intermediate Phase $La_{0.60}Ba_{0.40}MnO_3$. For the intermediate phase $La_{0.60}Ba_{0.40}MnO_3$, the intense reflections are again those of the perovskite subcell. Apart from those, one observes additional reflections belonging to different variants. A first system of reflections shows that at least one part of the sample exhibits the R-type lattice with $a_H \approx c_H \approx a_c\sqrt{2}$ and $b_H \approx 2a_c\sqrt{3}$ (the index H refers to the hexagonal indexation of this phase). However, these reflections are extremely weak, sometimes barely visible (as in the $[001]_c$ ED pattern of Figure 4a), so that it is not possible to differentiate the conditions limiting the reflection in the $R\bar{3}c$ space group from those of the *Imma* (and *I*4/*mcm*) space groups.

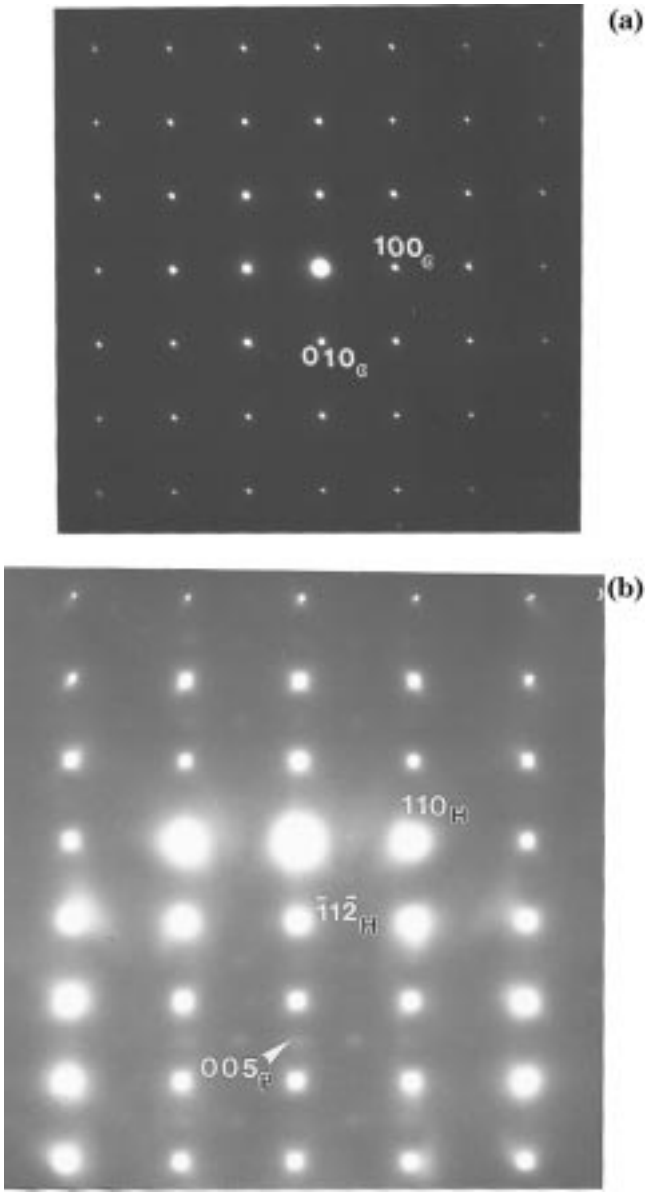

Figure 6. ED pattern of the perovskite $La_{1-x}Ba_xMnO_3$. **6a**: $[001]_P$ of $La_{0.6}Ba_{0.4}MnO_3$. **6b**: $R\bar{3}c$ and P-type double-cell ED patterns.

A second system of very weak reflections are observed, they are those of the P-type double cell. This is illustrated by the ED pattern of Figure 6. The crystal is slightly tilted around the $[110]_P$* axis, to enhance the phenomenon; this ED pattern appears very similar to that in Figure 3b; it differs only by the weakness of the additional reflections.

Magnetotransport Properties

The magnetization curves $M(T)$ registered in a magnetic field of 100 G for $Pr_{1-x}Ba_xMnO_3$ (Figure 7a) and for $La_{1-x}Ba_xMnO_3$ (Figure 8a) show clearly a transition from a paramagnetic (PM) to a ferromagnetic (FM) state

(9) Chapman, J. P.; Attfield, J. P.; Beales, T. P. *Angew. Chem.* **1996**, *35*, 2482.

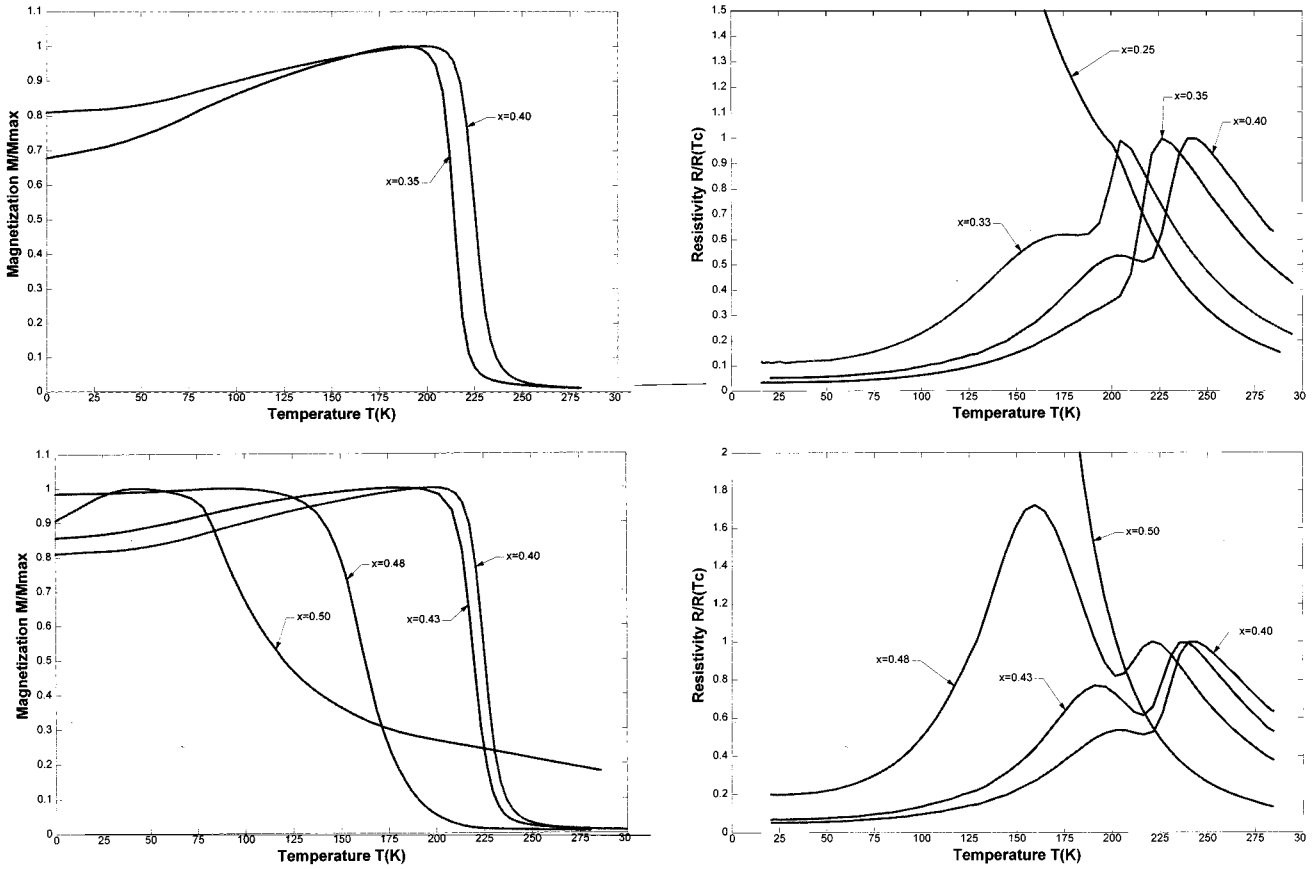

Figure 7. Physical properties of $Pr_{1-x}Ba_xMnO_3$. **7a** (left, top and bottom): Normalized magnetization curves versus temperature. **7b** (right, top and bottom): Normalized resistivity curves versus temperature.

at decreasing temperature. This type of transition has already been observed in other manganites such as $Ln_{1-x}Ca_xMnO_3$ (Ln = La,[10] Pr,[11−13] Nd,[14] Tb, Ho, or Y[15]) and $Ln_{1-x}Sr_xMnO_3$ (Ln = La,[16−17] Pr[18]). However in the present barium-based manganites several original features are observed:

(i) The Curie temperature of these manganites are significantly higher than those observed for other manganites. This is especially the case for the lanthanum phases which exhibit the highest T_C known to date for the manganites, with a maximum value of 362 K for $x = 0.35$.

(ii) The evolution of T_C is remarkable as shown in Table 2. In both series, T_C increases as x increases from $x = 0.10-0.20$, obtains a maximum at $x = 0.40$ for Pr and $x = 0.32$ for La, and then decreases again. Such an unusual evolution of T_C can easily be explained by taking into consideration three factors that have previously been shown to govern the magnetoresistance properties of these materials: the average size of the interpolated cation represented by the ionic radii $\langle r_A \rangle$,[19] the hole carrier density represented by the Mn^{4+} content which is termed "the valence effect",[20] and the size difference between the A site cations, "the mismatch effect", represented by the variance of the A-cation size radius distribution σ^2.[21] For each of the present Ba-based manganites, it appears clearly that $\langle r_A \rangle$ increases dramatically as x increases and contributes to the increase of T_C. Simultaneously however, the Mn^{4+} content and the variance σ^2 also increase with x so that these two factors contribute to the decrease of T_C as previously shown.[22,23] Thus at low x values the size effect $\langle r_A \rangle$ prevails with respect to the valence and mismatch effect whereas at higher x values, these two latter effects are predominant, leading finally to a decrease of T_C. The fact that the praseodymium phases exhibit a T_C about 100 K smaller than the lanthanum manganite for the same x value (see Table 2) is in agreement with these considerations since the Pr phases

(10) Mahendiran, R.; Mahesh, R.; Raychaudhuri, A. K.; Rao, C. N. R. *Solid State Commun.* **1995**, *94*, 7, 515−518.
(11) Tomioka, Y.; Asamitsu, A.; Kuwahara, H.; Moritomo, Y. *Phys. Rev. B* **1996**, *53*, 1689.
(12) Tomioka, Y.; Asamitsu, A.; Moritomo, Y.; Tokura, Y. *J. Phys. Soc. Jpn.* **1995**, *64*, 3626−3630.
(13) Lees, M. R.; Baratt, J.; Balakrishnan, G.; D. McPaul, K.; Yethiraj, Y. *Phys. Rev. B Condensed Matter* **1995**, *52*, 20.
(14) Liu, K.; Wu, X. W.; Ahn, K. H.; Sulchek, T.; Chien, C. L.; Xiao, J. Q. *Phys. Rev. B* **1996**, *54*, 3007.
(15) Kobayashi, T.; Takizawa, H.; Endo, T.; Sato, T.; Shimada, M.; Taguchi, H.; Nagao, M. *J. Solid State Chem.* **1991**, *92*, 116−129.
(16) Urushibara, A.; Moritomo, Y.; Arima, T.; Asamitsu, A.; Kido, G.; Tokura, Y. *Phys. Rev. B* **1995**, *51*, 14103.
(17) Mitchell, J. F.; Argyriou, D. N.; Potter, C. D.; Hinks, D. G.; Jorgensen, J. D.; Bader, S. D. *Phys. Rev. B* **1995**, *54*, 6172.
(18) Knizek, K.; Jirak, Z.; Pollert, E.; Zounova, F.; Vratislav, S. *J. Solid State Chem.* **1992**, *100*, 292−300.
(19) Sundaresan, A.; Maignan, A.; Raveau, B. *Phys. Rev. B*, in press.
(20) Maignan, A.; Simon, C.; Caignaert, V.; Raveau, B. *Z. Phys. B* **1996**, *99*, 305−310.
(21) Rodriguez-Martinez, L. M.; Attfield, J. P. *Phys. Rev. B* **1996**, *54*, 1.
(22) Raveau, B.; Maignan, A.; Caignaert, V. *J. Solid State Chem.* **1995**, *117*, 424.
(23) Hwang, H. Y.; Cheong, S. W.; Radaelli, P. G.; Marezio, M.; Batlogg, B. *Phys. Rev. Lett.* **1995**, *74*, 914.

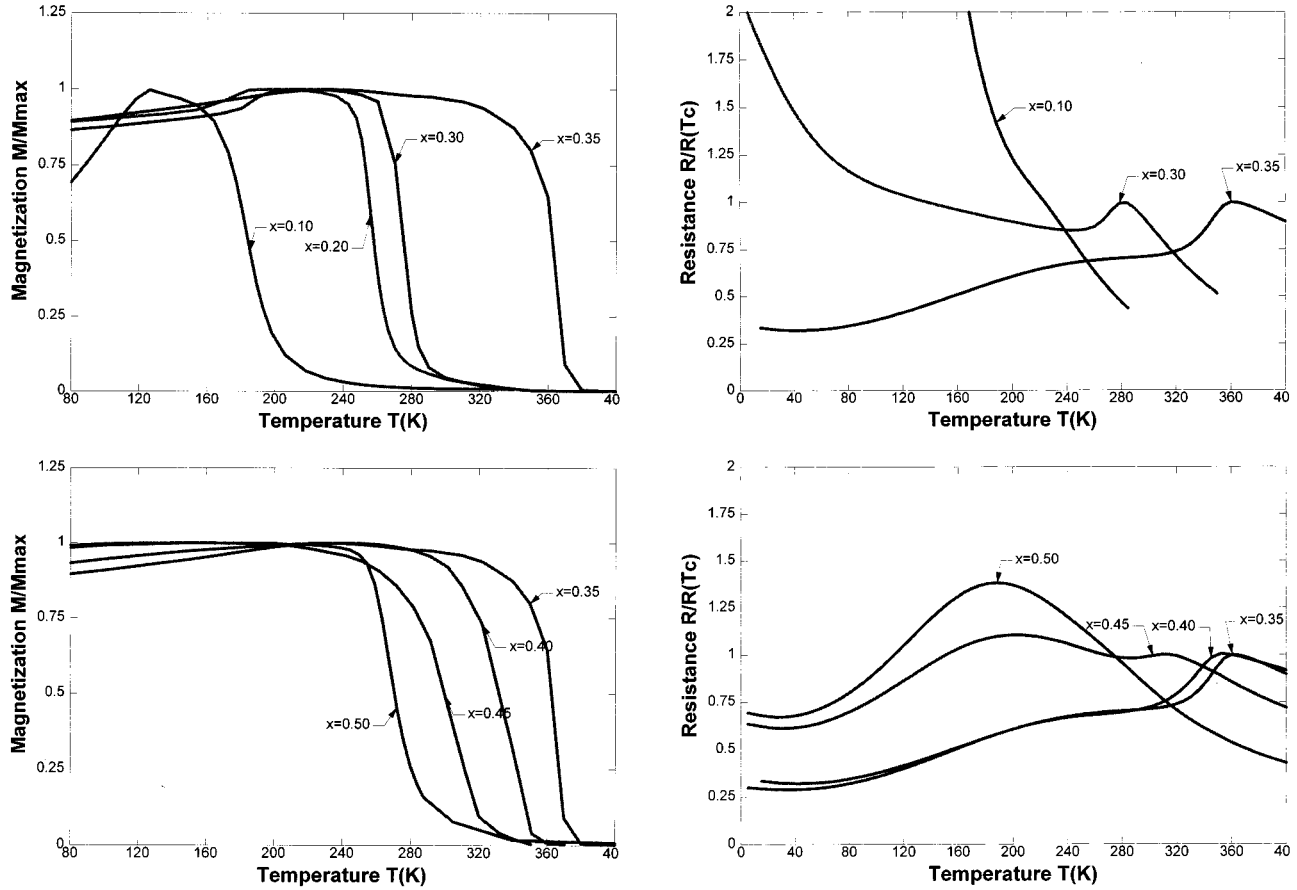

Figure 8. Physical properties of $La_{1-x}Ba_xMnO_3$. **8a** (left, top and bottom): Normalized magnetization curves versus temperature. **8b** (right, top and bottom): Normalized resistivity curves versus temperature.

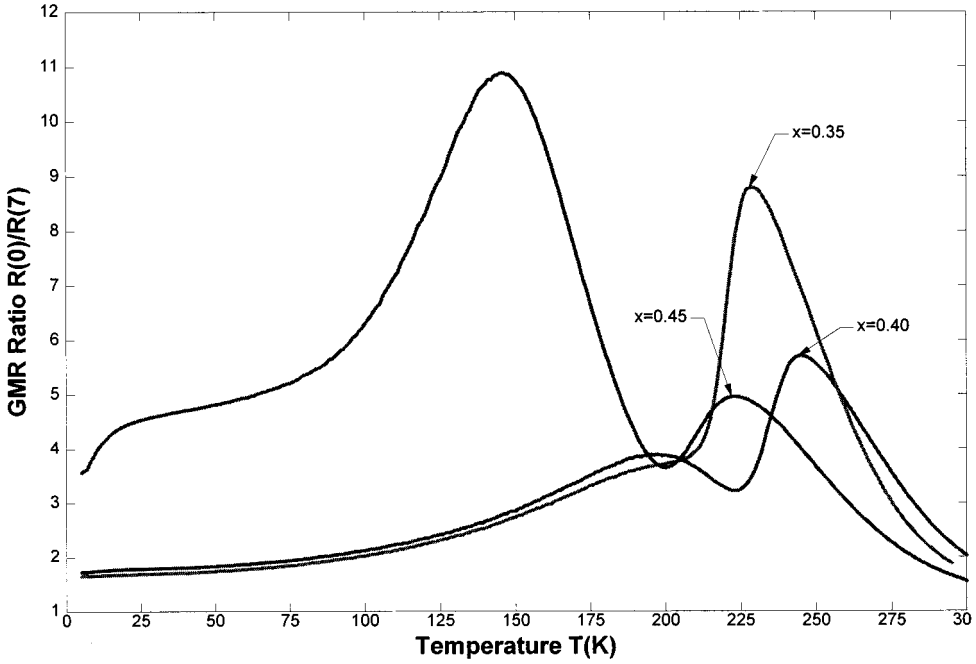

Figure 9. Resistance ratio $R_{(0T)}/R_{(7T)}$ versus temperature for the $Pr_{1-x}Ba_xMnO_3$ system.

exhibit a higher σ^2 variance and a smaller $\langle r_A \rangle$ which both favor a decrease of T_C.

The resistance curves $R(T)$ (Figures 7b and 8b) shown for a great number of compositions, a peak characteristic of a metal-to-insulator (MI) transition at increasing temperature. For those compositions, one observes that the temperature T_m of the MI transition coincides with T_C (see Table 2) so that these compounds can be expected to exhibit CMR properties. Resistance measurements performed in a magnetic field of 7 T confirms this hypothesis; this is evident from the plot of the R_0/R_7 ratio versus temperature for several praseodymium phases $Pr_{1-x}Ba_xMnO_3$ (Figure 9). Note however that the magnetoresistance effect is not high, resistance ratio

Table 2. Curie Temperatures

$Pr_{1-x}Ba_xMnO_3$ Series

x	0.25	0.33	0.35	0.40	0.43	0.45	0.48	0.50
T_m [$R(T)$]	SC	205	228	242	238	222		SC
T_C [$M(T)$]	180	208	218	235	225	210	166	90

$La_{1-x}Ba_xMnO_3$ Series

x	0.10	0.20	0.30	0.35	0.40	0.45	0.50
T_m [$R(T)$]	SC		282	358	350	312	265
T_C [$M(T)$]	185	258	275	362	332	300	272

reaching only a maximum value of 9. Moreover it must be pointed out that the $R(T)$ curves are more complex than for other manganites since a second peak, or at least a bump, appears at low temperature especially in the case of the praseodymium phases (Figure 7b) whose origin has not been explained to date.

Finally, no clear influence of the structure upon the magnetoresistance properties of these compounds could be detected. Nevertheless, it is worth pointing out that one observes a FMM−PMI transition whatever the nature of the perovskite structure. An accurate structure determination, using neutron diffraction would be necessary to understand the relationship between the distortion of the octahedra and the magnetoresistance properties in these compounds, and to precise the eventual influence of Jahn−Teller effect on these properties.

Concluding Remarks

The reinvestigation of the $Ln_{1-x}A_xMnO_3$ systems with Ln = Pr, La using a new synthesis route has allowed us to extend the homogeneity range of these perovskites up to $x = 0.60$ and $x = 0.50$ for Pr and La, respectively. Two new perovskites, a cubic form and a P-type tetragonal phase characterized by a doubling of one parameter ($a_C \times a_C \times 2a_C$) have been evidenced. The HREM study shows the complex crystal chemistry of these compounds especially of the new tetragonal form which is stabilized only in small domains and coexists coherently in the same matrix with either the *Imma* perovskite (Pr) or with the $R\bar{3}c$ perovskite (La). The first important feature that characterizes the magnetoresistance properties of these compounds is that they exhibit a ferromagnetic metallic-to-paramagnetic insulating transition at increasing temperature, over a large homogeneity range, independent of the nature of the perovskite structure. Consequently, magnetoresistance effects are observed, though the resistance ratio remain modest. The second important point deals with the Curie temperature which reaches values as high as 362 K and goes though a maximum due to a beating of three factors—size, valence and mismatch effects—which are known to govern the CMR properties of all the manganites.

CM9704084